THE ASTROPHYSICAL JOURNAL, 518:457–472, 1999 June 10

THE COSMIC-RAY PROTON AND HELIUM SPECTRA BETWEEN 0.4 AND 200 GV

M. BOEZIO, P. CARLSON, T. FRANCKE, AND N. WEBER
Royal Institute of Technology (KTH), S-104 05 Stockholm, Sweden

M. SUFFERT
Centre des Recherches Nucléaires, BP20, F-67037 Strasbourg-Cedex, France

M. HOF, W. MENN, AND M. SIMON
Universität Siegen, 57068 Siegen, Germany

S. A. STEPHENS
Tata Institute of Fundamental Research, Bombay 400 005, India

R. BELLOTTI, F. CAFAGNA, M. CASTELLANO, M. CIRCELLA, AND C. DE MARZO
Dipartimento di Fisica dell'Università and Sezione INFN di Bari, Via Amendola 173, I-70126 Bari, Italy

N. FINETTI, P. PAPINI, S. PICCARDI, AND P. SPILLANTINI
Dipartimento di Fisica dell'Università and Sezione INFN di Firenze, Largo Enrico Fermi 2, I-50125 Firenze, Italy

M. RICCI
Laboratori Nazionali INFN, Via Enrico Fermi 40, CP 13, I-00044 Frascati, Italy

M. CASOLINO, M. P. DE PASCALE, A. MORSELLI, P. PICOZZA, AND R. SPARVOLI
Dipartimento di Fisica dell'Università and Sezione INFN di Roma, Tor Vergata, Via della Ricerca Scientifica 1, I-00133 Roma, Italy

G. BARBIELLINI, U. BRAVAR, P. SCHIAVON, A. VACCHI, AND N. ZAMPA
Dipartimento di Fisica dell'Università and Sezione INFN di Trieste, Via A. Valerio 2, I-34147 Trieste, Italy

J. W. MITCHELL, J. F. ORMES, AND R. E. STREITMATTER
Code 661, NASA/Goddard Space Flight Center, Greenbelt, MD 20771

AND

R. L. GOLDEN[1] AND S. J. STOCHAJ
Box 3-PAL, New Mexico State University, Las Cruces, NM 88003
Received 1998 April 27; accepted 1999 January 19

ABSTRACT

We report on the hydrogen nuclei (protons and deuterons) spectrum from 0.15 to 200 GeV and on the helium nuclei spectrum over the energy range from 0.2 to 100 GeV nucleon^{-1} at the top of the atmosphere measured by the balloon-borne experiment Cosmic Antiparticle Ring-Imaging Cerenkov Experiment (CAPRICE), which was flown from Lynn Lake, Manitoba, Canada, on 1994 August 8–9. We also report on the proton spectrum over the energy range from 0.15 to 4.2 GeV. The experiment used the NMSU-WiZard/CAPRICE balloon-borne magnet spectrometer equipped with a solid radiator Ring-Imaging Cerenkov (RICH) detector and a silicon-tungsten calorimeter for particle identification. This was the first time a RICH was used together with an imaging calorimeter in a balloon-borne experiment. These detectors allowed for clear particle identification, as well as excellent control of the detector efficiencies. The data were collected during 18 hr at a residual mean atmospheric depth of 3.9 g cm^{-2}. With this apparatus 516,463 hydrogen and 32,457 helium nuclei were identified in the rigidity range 0.4 to 200 GV and 1.2 to 200 GV, respectively. The observed energy spectrum at the top of the atmosphere can be represented by $(1.1 \pm 0.1) \times 10^4\ E^{-2.73 \pm 0.06}$ particles (m^2 GeV sr s)$^{-1}$ for hydrogen (E in GeV) between 20 and 200 GeV and $(4.3 \pm 0.9) \times 10^2\ E^{-2.65 \pm 0.07}$ particles (m^2 GeV nucleon^{-1} sr s)$^{-1}$ for helium nuclei (E in GeV nucleon^{-1}) between 10 and 100 GeV nucleon^{-1}. These spectra are in good agreement with other recent measurements above 10 GeV. The observed spectra flatten below 10 GeV due to solar modulation and are consistent with earlier measurements when solar modulation is taken into account. Between 5 and 200 GV the hydrogen to helium ratio as a function of rigidity was found to be approximately constant at 6.1 ± 0.1.

Subject headings: cosmic rays — elementary particles

1. INTRODUCTION

Protons and helium nuclei are the dominant components of cosmic rays. A precise knowledge of their fluxes as a function of energy—the spectra—of these particles is important for several reasons. The interstellar spectra, which in principle can be derived from the measurements at the top of the Earth's atmosphere by demodulating the observed spectra for solar modulation, are important in understanding the Galactic propagation and acceleration mechanisms of cosmic rays. Since protons and helium nuclei at a fixed rigidity have different momenta and kinetic energies per nucleon, the comparison of their spectra provides useful constrains for modulation and acceleration theories.

The fluxes of protons and helium nuclei entering the atmosphere give rise to many secondary particles. The neutrino, the decay product of the muon or of the pion, is of special interest in view of the so-called "atmospheric neu-

[1] Deceased.

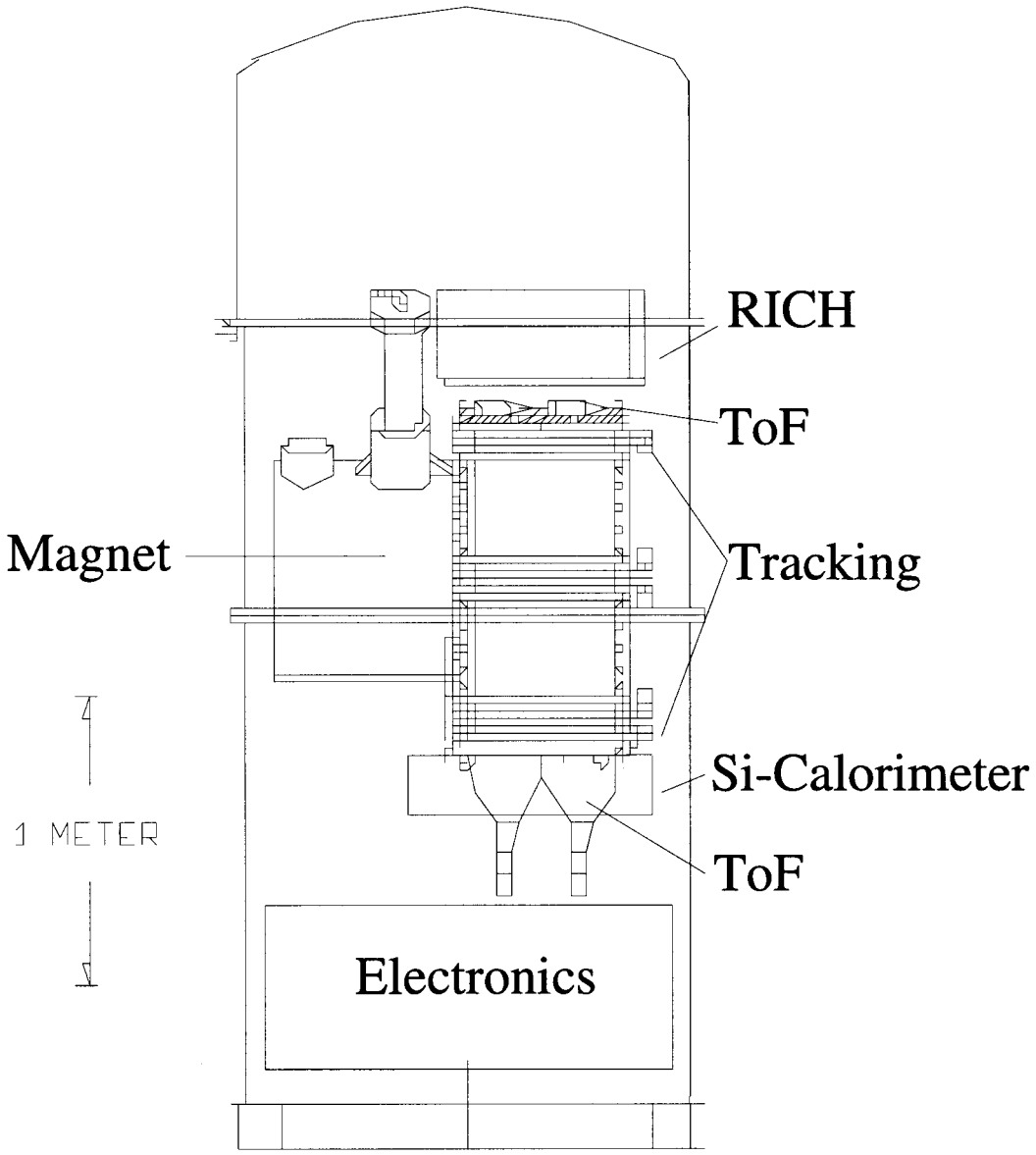

FIG. 1.—Schematic view of the CAPRICE apparatus

trino anomaly" (see, e.g., Gaisser et al. 1996). A precise knowledge of the primary flux helps in reducing the uncertainty in the neutrino flux calculation (see, e.g., Circella et al. 1997). This is of the greatest importance for understanding the apparent deficit of muonlike neutrinos in underground neutrino detection experiments.

For energies above 10 GeV, where the effect of the solar modulation is less than about 10%, flux data published before 1995 differed by as much as a factor of 2 (Gaisser & Schaefer 1992 and Seo et al. 1991). The differences are probably due to imprecise or incomplete knowledge of detectors efficiencies. More recent experiments have been able to measure the efficiencies with greater care. These experiments report proton and helium nuclei spectra that show better agreement (Menn et al. 1997 and this work).

In this paper we report on the proton, hydrogen (proton and deuteron), and helium nuclei spectra measured with the Cosmic Antiparticle Ring-Imaging Cerenkov Experiment (CAPRICE) 1994 balloon experiment. For protons, we give results in the rigidity range from 0.4 to 5 GV, for hydrogen nuclei from 0.4 to 200 GV, and for helium nuclei from 1.2 to 200 GV. The CAPRICE experiment was unique in providing three excellent particle identification detectors: a time-of-flight system, a Ring-Imaging Cerenkov (RICH) detector, and an imaging calorimeter. With these independent detectors, it was possible to accurately determine the efficiency and rejection power of each detector by selecting event samples using subsets of these detectors.

Preliminary results from this experiment were reported earlier (Barbiellini et al. 1997a). In this paper the CAPRICE detector system is described in § 2, the data analysis is described in § 3, and the results are discussed in § 4.

2. DETECTOR SYSTEM

Figure 1 shows the NMSU-WiZard/CAPRICE spectrometer that was flown by balloon from Lynn Lake, Manitoba, Canada (56°.5 north latitude, 101°.0 west longitude), to Peace River, Alberta, Canada (56°.15 north latitude, 117°.2 west longitude), on 1994 August 8 and 9 at an atmospheric pressure of 3.2 to 4.5 mbar (altitude of 36.0–38.1 km) for 23 hr. It included from top to bottom: a RICH detector, a time-of-flight (TOF) system, a superconducting magnet

spectrometer equipped with multiwire proportional chambers (MWPC) and drift chambers (DC), and a silicon-tungsten imaging calorimeter. In the CAPRICE experiment, particular emphasis was put on particle identification. The aim was to achieve the ability to safely reject protons (rejection factor $\sim 10^6$) against positrons (Barbiellini et al. 1996b) and e^-, μ^-, and π^- against $\bar{p}$ (Boezio et al. 1997), as well as to separate light isotopes.

The 50×50 cm^2 RICH detector (Carlson et al. 1994; Barbiellini et al. 1996a), with a threshold Lorentz factor of 1.5, used a solid NaF radiator and a photosensitive MWPC with pad readout to detect the Cerenkov light image and hence measure the velocity of the particles. The time-of-flight system had two layers, each layer made of two 1 cm thick 25×50 cm^2 paddles of plastic scintillator, one above and one below the tracking stack. Each paddle was equipped with two 5 cm diameter photomultiplier tubes, one at each end. The time-of-flight system was used to give a trigger, to measure the time-of-flight over a 1.1 m path length, and to measure the ionization (dE/dX) losses of the particles. The spectrometer consisted of a superconducting magnet, multiwire proportional chambers, and drift chambers (Golden et al. 1978, 1991; Hof et al. 1994). The magnet was comprised of a single coil of 11,161 turns of copper-clad NbTi wire. The outer diameter of the coil was 61 cm and the operating current was 120 A, producing an inhomogeneous field of $\sim 4T$ at the center of the coil. The spectrometer provided 19 position measurements (12 DC and seven MWPC) in the bending direction (x) and 12 measurements (eight DC and four MWPC) in the nonbending direction (y). Using the position information together with the map of the magnetic field, we determined the rigidity of the particle. Figure 2 shows the distribution of the deflection uncertainty for protons. The deflection uncertainty is obtained on an event-by-event basis during the fitting procedure (see Golden et al. 1991 for a description how this quantity is computed and related to the errors on the measurements). From this distribution an average maximum detectable rigidity (MDR) of 175 GV is obtained.

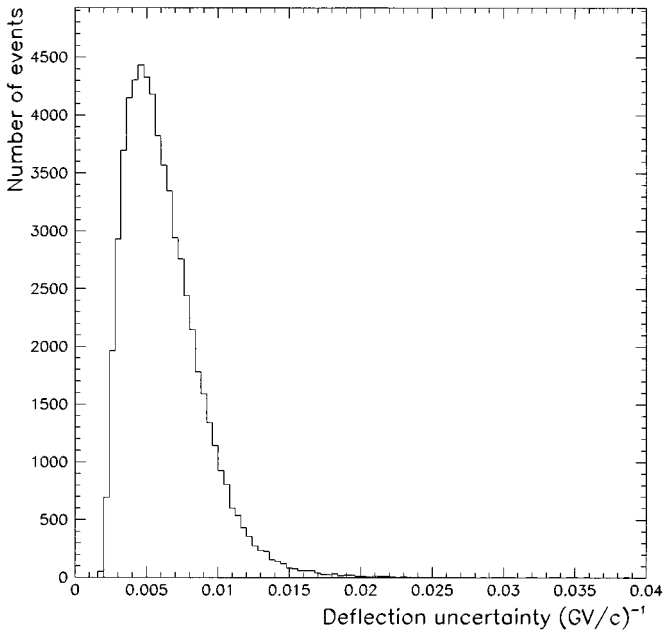

FIG. 2.—Distribution of the deflection uncertainty for protons

Finally, the electromagnetic calorimeter (Bocciolini et al. 1996) consisted of eight 48×48 cm^2 silicon planes, giving both x and y projection readouts. These silicon planes were interleaved with tungsten converters one radiation length thick. The segmentation of the silicon planes into strips provided information on the longitudinal and lateral profiles of the interactions along with the total deposited energy.

3. DATA ANALYSIS

The analysis was based on 60,520 s of data taken over a total acquisition time of 18 hr under an average residual atmosphere of 3.9 g cm^{-2}.

Protons are the most common singly charged positive particles in the cosmic radiation, with a few percent admixture of deuterons (Reimer et al. 1995) and an even smaller fraction of positrons (Barbiellini et al. 1996b). After protons, helium nuclei are the most abundant particles in the cosmic radiation. In measurements made with balloon-borne instruments there is also a small, but not negligible, contribution of secondary particles produced in the residual atmosphere above the instrument, as well as in the instrument itself. In the case of positive particles, these are mainly protons, muons, pions, and positrons.

The NMSU/WiZard-CAPRICE instrument was able to distinguish among different particles using the scintillators (dE/dX and time of flight), the calorimeter, and the RICH independently. This unique feature of the apparatus allowed clean samples of various particles to be selected by subsets of these detectors, making it possible to accurately determine the rigidity-dependent efficiency and rejection power of each individual detector. This capability is unique in the CAPRICE experiment.

In the rigidity interval from 0.4 to 5 GV, protons could be separated from deuterons. At higher rigidities, from 5 to 200 GV, protons and deuterons could not be separated and therefore the hydrogen nuclei flux was measured. All selected $Z = 1$ particles (hydrogen nuclei, which include deuterons) were treated as being protons in this analysis. Helium nuclei could be identified between 1.2 and 200 GV. The upper rigidity limit was set by the maximum detectable rigidity (MDR), which, although position dependent, had an average value of 175 GV. No attempt was made in this paper to separate between ^{3}He and ^{4}He nuclei, although separation is possible between 1 and 4 GV (Barbiellini et al. 1997b). Hence, in the analysis all $Z = 2$ particles were treated as being ^{4}He.

3.1. *Particle Selection*

3.1.1. *Albedo Particles*

Downward moving particles were selected using the time-of-flight information. The time-of-flight resolution of 280 ps, which was small compared to the flight time of more than 4 ns, assured that no contamination from albedo particles remained in the selected sample. Reentrant albedo particles, i.e., albedo particles produced in the opposite hemisphere that were bent back into the atmosphere by the Earth magnetic field, were not considered to be a problem since the measurements presented in this paper are above the geomagnetic cutoff.

3.1.2. *Tracking*

The tracking information was used to determine the rigidity of the particles. To achieve a reliable estimation of

the rigidity, a set of conditions was imposed on the fitted tracks, partly based on the experience gained previously using the same tracking system (Mitchell et al. 1996; Hof et al. 1996)

1. At least 12 (out of 19) position measurements in the bending (x) direction and seven (out of 12) in the nonbending (y) direction were required.
2. An acceptable χ^2 for the fitted track.
3. The estimated error on the deflection should be less than 0.02 $(GV)^{-1}$.

These conditions also eliminated events with more than one track in the spectrometer.

3.1.3. *Scintillators and Time of Flight*

Figure 3 shows the ionization loss (dE/dX) in the top scintillator as a function of magnetic deflection (reciprocal of rigidity, $1/R$) for all positive particles ($\sim$714,000 events) passing the tracking selection criteria. The dE/dX was measured in units of most probable signal of a minimum ionizing particle (mip). From the bottom of this figure to the top, one can see the bands of particles from minimum ionizing particles (muons, positrons, and pions), protons, deuterons, and helium nuclei. Particles with charge one were selected using the measured energy loss in the top scintillator. To select particles with charge two, both the top and bottom scintillators were used. The solid line in Figure 3 shows the upper limit used for the selection of charge one particles. It was a trade off between keeping as many deuterons as possible in the hydrogen sample and efficiently rejecting all charge two particles from the sample. In the same way the dashed lines in Figure 3 show the region used to select charge two particles. The rather strong selection criteria on the dE/dX signal in the top scintillator at low deflection values, as shown by the solid line in Figure 3, were used to eliminate multiple track events with more than

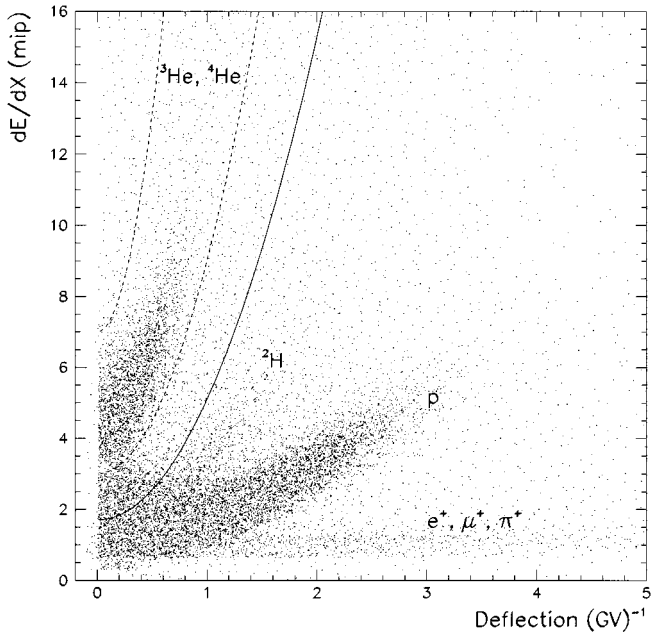

FIG. 3.—Ionization loss in the top scintillator as a function of deflection in the magnetic field for all positive particles passing the tracking selection criteria ($\sim$648,000 charge one and $\sim$66,000 charge two events). The solid and dashed lines show the selection criteria for $Z = 1$ and $Z = 2$ particles, respectively.

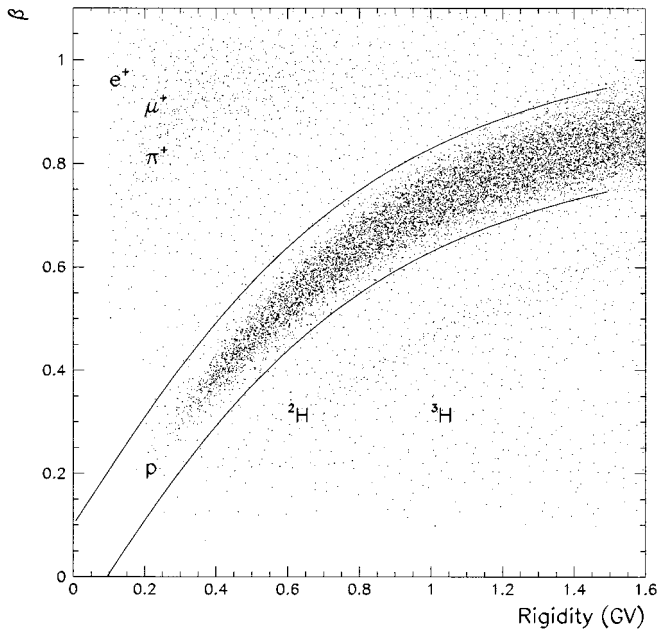

FIG. 4.—β calculated from the time of flight as a function of rigidity for all positive charge one particles passing the tracking selection criteria ($\sim$290,000 events, mostly protons). The solid lines show the selection criteria for protons.

one charged particle produced by interactions above the tracking system. Multiple track events were also rejected by requiring that not more than one of the two top scintillator's paddles was hit. The same requirement was applied to the bottom scintillators to assure a reliable time-of-flight information.

The time-of-flight information was used below 1.5 GV to select protons and hydrogen nuclei. The velocity (β) of the particle from the time of flight was compared to the β obtained from the fitted deflection assuming that the particle had the mass of a proton and the difference was required to be less than 2 σ. Above 1.5 GV, protons could not be distinguished from lighter particles using the time of flight. Figure 4 shows the time of flight measured by the two scintillators for all unit charge positive particles that pass the tracking selection. From left to right in this figure, one can see the bands corresponding to light particles (positrons, muons, and pions), protons, and deuterons. The solid lines show the band taken as protons based on less than 2 σ from the expected value. Hydrogen nuclei were selected using only the upper limit to reject $\beta \sim 1$ particles.

3.1.4. *RICH*

The RICH was used to measure the Cerenkov angle of the particle and thereby its velocity. Figure 5 shows the Cerenkov angle as a function of rigidity for unit charge positive particles passing the tracking selection. One can clearly identify the different particle types as indicated in this figure.

The velocity and incidence angle–dependent Cerenkov angle resolution was determined using a large number ($\sim$100,000) of protons selected by the calorimeter and the scintillators. For the proton and hydrogen nuclei identification the following selection criteria were used (Weber 1997)

1. A good agreement between the particle impact position as determined by the RICH and the tracking system

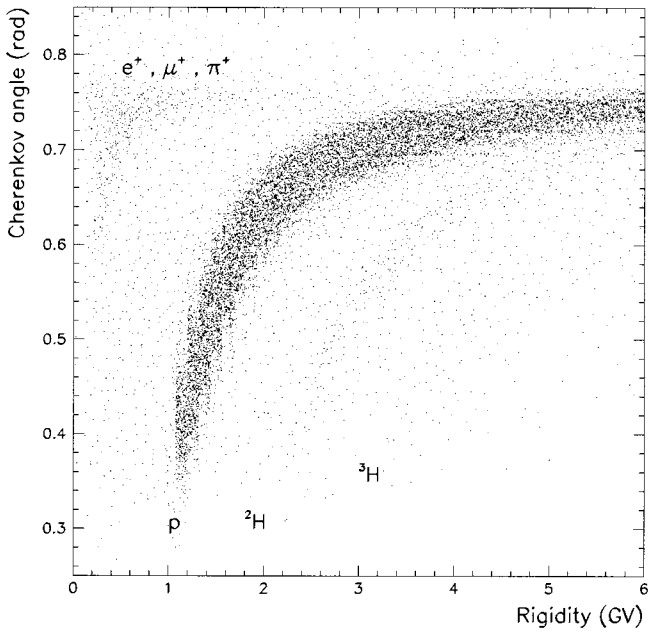

FIG. 5.—Reconstructed Cerenkov angle as a function of rigidity for positive charge one particles passing the tracking, scintillator, and RICH selection criteria (~279,000 events, mostly protons).

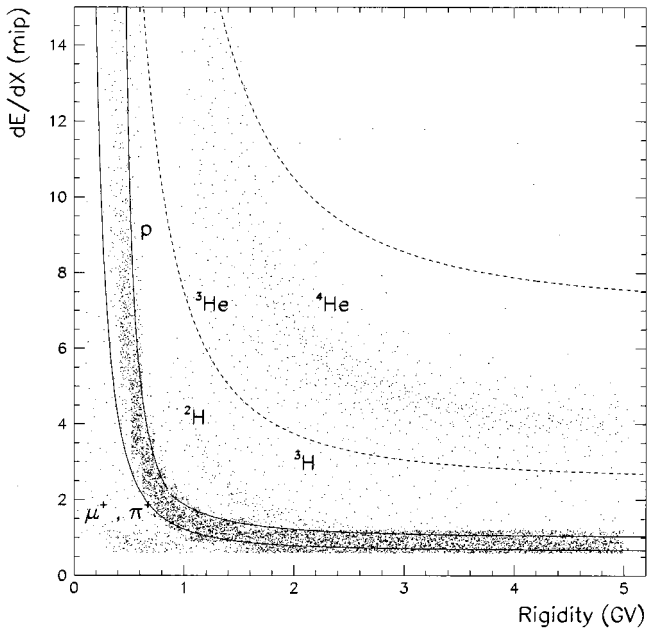

FIG. 6.—Average energy loss in the calorimeter as a function of rigidity for all noninteracting (in the calorimeter) positive particles passing the tracking criteria (~282,000 events of which ~268,000 are protons and ~9000 are charge two particles). The proton and helium nuclei selection criteria are marked by the solid and dashed lines, respectively.

was required. The difference in x and y, which was rigidity dependent but typically less than 5 mm, should be less than 3 σ.

2. Charged particles produced significantly higher signals than Cerenkov photons. This was used to reject events with multiple charged particles traversing the RICH by requiring that there was only one cluster of pads with high signals.

3. More than eight pads (approximately three to four photon electrons) were required to be used in the fit of the Cerenkov angle.

4. The reconstructed Cerenkov angle should not deviate by more than 3 σ from the expected Cerenkov angle for protons.

Using these conditions, we obtained reliable Cerenkov angle information. Criterion 2 was introduced to eliminate events with more than one charged particle crossing the RICH and, as well as criterion 1, was applied over the entire rigidity range both for the proton and the hydrogen nuclei selection. Criteria 3 and 4 were used to separate protons from deuterons and other particles and were used only in the rigidity range from 1.2 to 5 GV. Above 1.2 GV the efficiency of the RICH selection was higher than 50% for protons. Above 5 GV the difference between proton Cerenkov angle and that of deuterons becomes less than 3 σ. The RICH was not used in the helium nuclei selection.

3.1.5. *Calorimeter*

The calorimeter was used to identify protons and helium nuclei using the energy loss in the silicon detectors. Figure 6 shows the distribution of the average energy loss in the calorimeter as a function of rigidity for all positive particles selected in the rigidity range 0.4 to 5 GV, after the tracking selection. Only events with a single noninteracting particle in the calorimeter are included. Furthermore, the number of silicon strips hit by these noninteracting particles had to be greater than the minimum (rigidity dependent) number determined for protons. The average energy loss in the calorimeter was defined as the sum of the detected energy (in units of mip) of the five (or all if the number of planes hit was less than five) planes with the smallest signal out of a maximum 16, divided by the number of planes used in the sum. In Figure 6 a clear separation between protons and helium nuclei can be seen. Positrons were rejected by requiring that the incident particle did not interact in the calorimeter. Muons and pions show up with small average deposited energy and could be rejected up to 1.3 GV. One can also see in Figure 6 the band corresponding to ^{2}H nucleus. The selection criteria for the protons and helium nuclei are marked by the solid and dashed lines, respectively.

Because of its low efficiency, compared with the time of flight and the scintillator dE/dX selections, the calorimeter was only used to select proton and helium nuclei samples for efficiency studies of the other detectors.

3.1.6. *The Bar*

A 17 kg, 1.2 m long aluminum bar with a 7 kg steel swivel in the center, used to connect the payload to the balloon, was situated 2.3 m above the RICH. The production and loss of particles in the nonuniform I-shaped bar could not be estimated reliably, and hence it was chosen to reject all particles crossing it. This was done by extrapolating the tracks to the level of the bar. This resulted in a rigidity-dependent reduction of the geometrical factor of about 10%.

3.1.7. *Summary of the Selection Criteria for $Z = 1$ and $Z = 2$ Particles*

In summary, information from all detectors was used in the analysis to estimate the contamination and efficiency of each instrument. The particle fluxes presented below are based on the following particle-selection criteria:

1. The tracking system was used to select good events requiring a clean single track in the tracking system and crossing of the RICH and the calorimeter.
2. All the events with an extrapolated track crossing the bar that connects the payload to the balloon were rejected.
3. Selections based on the scintillator dE/dX were used to identify charge one and charge two particles.
4. The time of flight was used to reject albedo particles, to identify hydrogen nuclei, and to select protons up to 1.5 GV.
5. The RICH information was used for $Z = 1$ particles in the whole rigidity range as a position detector to eliminate scattered and interacting events and to separate protons from deuterons between 1.2 and 5 GV.

3.2. *Contamination*

The contamination of e^+, μ^+, π^+, deuterons, and heavier elements in the proton sample was carefully studied, as well as the unit charged particle contamination in the helium nuclei sample.

3.2.1. *Deuteron Contamination*

The deuteron contamination in the proton sample was small because of the low deuteron abundance in the cosmic radiation. Between 0.4 (below this rigidity deuterons range out in the instrument) and 1.5 GV, where the time of flight was used to identify protons, a sample of deuterons was selected using the dE/dX in the scintillators and in the calorimeter. The time-of-flight criteria, applied to this sample, resulted in a surviving fraction of deuteron of $0.3^{+0.2}_{-0.1}\%$. Between 1.2 and 3 GV, where the RICH was used to identify protons, a clean deuteron sample was selected by the calorimeter and the time of flight. The RICH criteria, applied to this sample, resulted in a surviving deuteron fraction of $(2.7 \pm 0.4)\%$. Thus, up to 3 GV the deuteron contamination in the proton sample was less than 0.1% assuming that the deuteron component is of the order of a few percent of the proton abundance. In the rigidity range 3 to 5 GV, only the RICH was able to separate between protons and deuterons. Here, the deuteron contamination could not be determined using independent samples selected by the other detectors, as was done at lower rigidities. However, because of the low abundance of deuterons and the strict criteria applied to the RICH data, it was assumed that the deuteron contamination in the proton sample was negligible in this rigidity range. Thus, it was possible to select a pure (contamination less than 0.1%) proton sample up to 5 GV and measure the proton spectrum from 0.4 to 5 GV. Above 5 GV rejection of deuterons was not possible; therefore, above 5 GV hydrogen nuclei were selected, which included deuterons, as is done in other experiments.

3.2.2. *Positron Contamination*

At rigidities above a few GV, the positron abundance in the data sample is negligible compared to the proton abundance (Golden et al. 1996). At lower rigidities, especially below 1 GV, the relative positron abundance, including the atmospheric contribution, increases and is of the same order as the muon abundance (Barbiellini et al. 1996b). However, as will be shown, the combined time of flight and RICH proton selection power greatly reduced this component and it could safely be assumed to be negligible. This was verified by selecting an electron sample using the calorimeter and applying the RICH and time-of-flight criteria on the sample.

3.2.3. *Muon and Pion Contamination*

The muon/pion contamination in the proton sample was studied using negatively charged muons recorded at ground before the flight. The surviving fraction of muons/pions was found to be $(0.21 \pm 0.04)\%$ between 0.4 and 1.2 GV, and $(0.45 \pm 0.05)\%$ between 1.2 and 3 GV, resulting in a muon contamination of the proton sample less than 0.1% in both rigidity ranges. Above 3 GV, muons (and pions) were not rejected in the proton and hydrogen nuclei selection. The estimated muon contamination at float altitude at 3 GV was only about 0.2%, and this contamination slowly decreases as the energy increases. Pions contribute only to a very small fraction of the muons above 3 GV (Stephens 1981). Thus, we neglect this contamination in our analysis.

3.2.4. *Helium Nuclei Contamination in the Proton and Hydrogen Nuclei Samples*

Heavier particles, mainly helium nuclei, were efficiently rejected by the scintillator dE/dX selection criteria. A test sample selected by the calorimeter shows that the contamination of heavier elements in the proton and hydrogen nuclei samples was less than 0.1% in the whole rigidity range.

3.2.5. $Z = 1$ *Particle Contamination in the Helium Nuclei Sample*

The contamination of charge one particles in the helium nuclei analysis was studied by selecting a sample of $Z = 1$ particles with the calorimeter. The dE/dX scintillator selection applied to this sample shows a negligible ($<0.1\%$) contamination.

3.3. *Efficiency*

As shown above, the corrections for contaminations in the proton, hydrogen, and helium nuclei samples, as well as the statistical uncertainties, are small. Therefore, it was important to accurately determine the efficiency of each detector, resulting from the particle-selection criteria invoked in the analysis, to accurately determine the fluxes of the different particle types. The sophisticated particle-identifying detectors used in this experiment made it possible to select clean and independent samples of different particle types to determine the efficiency of each detector. The resulting efficiencies for protons and helium nuclei as a function of rigidity are shown in Figures 7*a* and 7*b*, respectively, and are discussed in more detail below.

The efficiency of each detector was determined as a function of rigidity in a number of discrete bins. The efficiency was then parameterized to allow an interpolation between bins. This parameterization introduced a systematic error on the efficiency of each detector. Since the parameters were correlated, the error on the efficiency was obtained using the error matrix of the fit for each detector when correcting the measured flux for the detector efficiencies.

3.3.1. *Tracking Efficiency*

The tracking efficiency was obtained from test samples of protons and helium nuclei selected by combining the information of the other detectors.

The proton test sample was between 0.4 and 3 GV selected as events with a single track in the RICH and only one

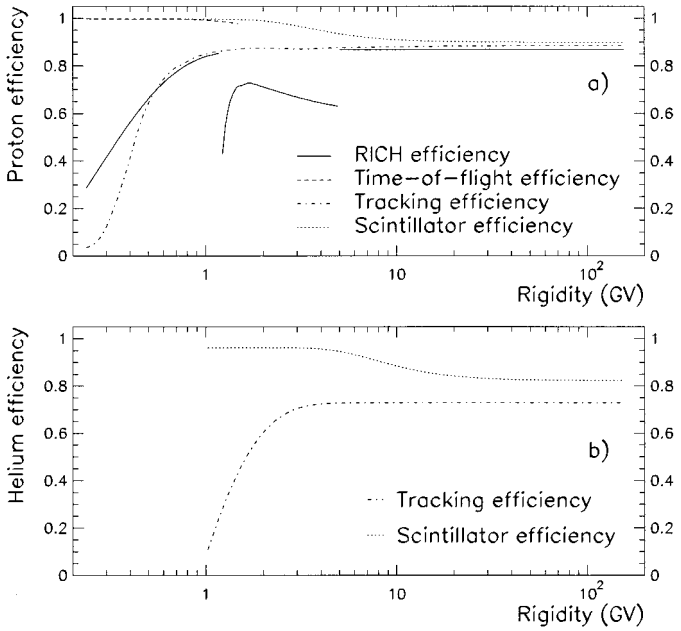

FIG. 7.—Selection efficiencies as a function of rigidity for (*a*) hydrogen nuclei and (*b*) helium nuclei.

paddle hit in the top and bottom scintillators. This sample was void of helium nuclei, and at low rigidities (below 1.5 GV) from deuterons, light particles, and showers of multiparticle events—removed by requiring a match between the dE/dX losses and the time of flight corresponding to a proton both in the top and in the bottom scintillators. Furthermore, the range in the calorimeter, i.e., the number of planes traversed by the particle, should match the expected track length of a proton. For rigidities above 700 MV (as determined from the time of flight assuming the mass of a proton) a single noninteracting track in the calorimeter was required. This track was then used to determine the position and the direction of the particle at the entrance of the calorimeter, and the particle trajectory was extrapolated, taking into account the magnetic field, to the position of the RICH using the rigidity obtained from the time of flight assuming that the particle had the mass of a proton. A loose match between the measured impact position in the RICH and the result of the extrapolated track was required. This further cleaned the sample from multiparticle showers but still kept events with multiple scattering in the test sample. The tracking selection criteria were applied to this sample to determine the tracking efficiency between 0.4 and 3 GV.

Above 3 GV a different method was used. A sample selected as described above was used to determine the efficiency of a very loose tracking criterion, namely, that the fitting routine converged but with no additional conditions on the tracking system. This efficiency was 97% at 3 GV. It was then assumed that this efficiency was constant at rigidities higher than 3 GV. The rigidity obtained using only this loose condition was the rigidity used when determining the total tracking efficiency, and the trajectory was used to require a loose match with the impact positions in the RICH and in the calorimeter. A proton test sample above 3 GV was then selected requiring only one charged particle in the RICH, only one paddle hit in the top and bottom scintillators, and a signal in both the top and the bottom scintillator corresponding to a minimum ionizing unit charge particle. The tracking selection criteria were then applied to the test sample and the resulting efficiency was multiplied by 0.97 to correct for the loose criteria already applied to the tracking system. In this way it was possible to determine the rigidity dependence of the tracking efficiency at all rigidities. A similar method was used to determine the tracking efficiency for helium nuclei with the difference that the selected particles were assumed to have the mass of ^{4}He.

The tracking efficiency for protons was slightly below 90%, as could be expected taking into account the individual chamber efficiencies, δ-ray production, scattering, etc. Above 3 GV a small increase in efficiency with increasing rigidity was found. Below 1 GV the efficiency sharply decreased mainly because of the cross talk in the drift chambers induced by high ionization. This effect was more important for the helium nuclei due to the higher ionization, and as a result the tracking efficiency was always lower than 80% for helium nuclei even at high energies.

The tracking efficiency was cross checked by comparing the hydrogen nuclei spectrum at the spectrometer obtained using the tracking system as a whole with the spectrum obtained using only the drift chamber information. In this last case, the tracking efficiency was determined with a hydrogen nuclei test sample selected by the scintillator dE/dX and the rigidity obtained by a fit to the MWPC information. Figure 8 shows the relative difference between the two resulting hydrogen nuclei spectra at the spectrometer. The good agreement between the two is a strong support for a reliable tracking efficiency estimation.

The methods described above require a discussion of possible systematic errors. For example, events that interacted in the calorimeter and produced particles that were scattered back into the tracking system were not part of the test sample and could affect the tracking efficiency. However,

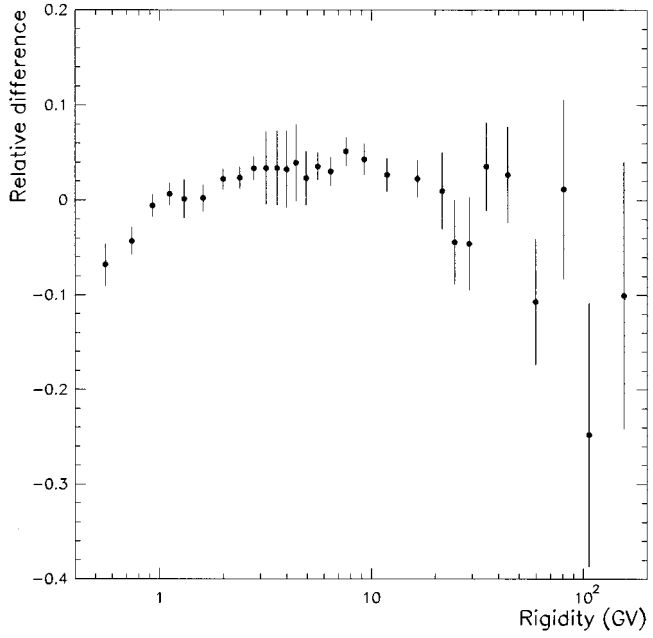

FIG. 8.—Difference between the hydrogen nuclei spectrum at the spectrometer obtained with track fit of the complete tracking system information and with track fit of only drift chamber information, normalized with the spectrum of the complete tracking system, as a function of rigidity.

most of these events were removed by the dE/dX, and time-of-flight selection and their effect were included in the efficiency of the scintillators. Furthermore, events with backscattering into the tracking system were studied on an event-by-event basis and no evidence was found that they would reduce the efficiency of the tracking system. From the good agreement between the two methods described above it was estimated that the tracking efficiency was determined with a precision of better than $\pm 5\%$. This uncertainty has not been added to the flux data but should be considered as part of an overall systematic error of the flux measurements presented in this paper (see the discussion of systematic errors below).

3.3.2. *Scintillator Efficiency*

A large proton sample (more than 100,000 events selected by the RICH and the calorimeter) was used to determine the scintillator dE/dX and time-of-flight efficiencies. Below 5 GV the contamination in the proton test sample was negligible ($<0.1\%$). Above 5 GV the test sample included an unknown contamination of deuterons. However, at rigidities above 5 GV the dE/dX and time-of-flight response of the scintillators was identical for protons and deuterons. The scintillator selection efficiency for charge two particles was determined using a helium nuclei sample selected by the calorimeter. The contamination in the test sample was negligible. The scintillator dE/dX efficiency, as shown in Figure 7 for both the proton and the helium nuclei selection, was high and, as expected, only weakly dependent on the rigidity. The decrease at high rigidities was due to the logarithmic rise of the dE/dX losses in the scintillators, which was not corrected for in the selection criteria.

3.3.3. *RICH Efficiency*

A large proton sample selected by the dE/dX in the scintillators, the time of flight, and the calorimeter was used to determine the efficiency of the RICH. The test sample had a negligible contamination up to 3 GV. Above 3 GV there was an unknown contamination of deuterons, which was assumed to be of the order of a few percent. This contamination will underestimate the RICH efficiency and a 2% systematic uncertainty has been added to the RICH efficiency due to the deuteron contamination between 3 and 5 GV where the RICH was used to select protons. Above 5 GV, where the RICH only was used as a veto against multiparticle events, the small deuteron component has no effect on the RICH efficiency since the response of the RICH at these rigidities was similar for protons and deuterons. The RICH was not used in the helium nuclei selection.

The RICH efficiency for protons between 1.2 and 5 GV was low close to the threshold to produce Cerenkov light because the number of Cerenkov photons emitted was small. The efficiency increased rapidly, reaching a value of 70% around 1.5 GV, followed by a slow decrease. Outside this rigidity range, the RICH was used as a charged particle position detector with an efficiency of about 85% above 5 GV. Below 1 GV the efficiency decreased because of increased multiple scattering in the RICH.

3.3.4. *Calorimeter Efficiency*

The calorimeter was used only to select test samples for determining the efficiencies of the other detectors. Since it was not used in the particle selection there was no need to determine its efficiency.

3.4. *Proton, Hydrogen, and Helium Nuclei Fluxes at the Top of the Atmosphere*

To obtain the proton, hydrogen, and helium nuclei fluxes at the top of the atmosphere several corrections must be made. The number of particles must be adjusted to account for secondary particles produced in the atmosphere and particles lost through interactions. In addition the measured energies must be corrected for ionization losses both in the instrument, above the spectrometer, and in the atmosphere above the payload.

Furthermore, the detector efficiencies, the geometrical factor (G), obtained with simulation techniques (Sullivan 1971), and the total live time have to be taken into account. The geometrical factor increased with rigidity from 130 cm^2 sr at 0.2 GV attaining a nearly constant value above 1 GV of 175 cm^2 sr. The fractional live time during the flight was 0.2690 ± 0.0006 resulting in a total live time (T_{live}) of $16{,}280 \pm 36$ s.

Since the detector efficiencies varied with rigidity it was important to properly define the rigidity values at which these efficiencies had to be estimated. The rigidity range was split in bins of 50 MV width, narrow enough so that the efficiencies did not vary appreciably inside each bin, up to 4 GV. Above 4 GV, bins with constant width in deflection, equal to half the most probable deflection uncertainty ($0.003\ \mathrm{GV}^{-1}$), were chosen. For each bin the number of particles was counted and corrected for the detector efficiencies.

All particles interacting in the spectrometer above the tracking system were assumed to be rejected by the selection criteria (see the discussion on systematic errors below). The data were corrected for the losses of these events with multiplicative factors that took into account the different materials in the detector using the expressions for the interaction mean free path given by Pfeifer, Roesler, & Simon (1996) and by Stephens (1997). The corrected number of protons, hydrogen, and helium nuclei at the top of the payload are given in Tables 1 and 2.

From the proton (hydrogen) numbers, the atmospheric secondary protons (Papini, Grimani, & Stephens 1996) were subtracted using a mean residual atmospheric depth of $3.9 \pm 0.4\ \mathrm{g\ cm}^{-2}$. The error includes a 10% uncertainty of the absolute calibration of the pressure gauge used to monitor the overlaying atmosphere.

Finally, the data were corrected for losses in the atmosphere above the detector due to interactions giving the number of protons (hydrogen) (N_p^{TOA}) and helium nuclei ($N_{\mathrm{He}}^{\mathrm{TOA}}$) at the top of the atmosphere. The differential fluxes as a function of kinetic energy per nucleon E are given by

$$\mathrm{Flux}_{p,\mathrm{He}}(E) = \frac{1}{T_{\mathrm{live}}\, G \Delta E}\, N_{p,\mathrm{He}}^{\mathrm{TOA}}(E)\,, \tag{1}$$

where ΔE is the energy bin corrected for ionization losses to the top of the atmosphere, either in kinetic energy in the case of proton (and hydrogen nuclei) or in kinetic energy per nucleon for helium nuclei. The resulting fluxes are given in Tables 3 and 4. Figure 9 shows the hydrogen and helium nuclei fluxes measured by this experiment at the top of the atmosphere. In Figure 10 we compare the CAPRICE fluxes with recent results from two previous balloon experiments using magnet spectrometers: Low Energy Antiproton (LEAP; Seo et al. 1991) and Isotope Matter Antimatter Experiment (IMAX; Menn et al. 1997) and from the RICH

TABLE 1

SUMMARY OF PROTON AND HYDROGEN NUCLEI RESULTS

RIGIDITY AT SPECTROMETER[a] (GV)	OBSERVED NUMBER OF EVENTS AT SPECTROMETER		EXTRAPOLATED NUMBER AT TOP OF PAYLOAD		ATMOSPHERIC CORRECTION	EXTRAPOLATED NUMBER OF PRIMARY EVENTS AT TOA[b]	
	p	H	p	H		p	H
0.4–0.6	18017	18112	42191	42542	13556	28641	28993
0.6–0.8	33168	33605	54570	55440	7975	46673	47544
0.8–1.0	40305	41045	59602	60772	4119	55882	57060
1.0–1.2	41411	42292	59708	60912	2694	58013	59238
1.2–1.4	25838	39868	56572	57641	2112	55976	57076
1.4–1.8	55316	68404	96585	99131	3032	97075	99718
1.8–2.2	42367	52791	75088	76814	1964	76129	77926
2.2–2.6	30733	39637	56615	58217	1319	57600	59269
2.6–3.0	23009	30265	43872	44930	916	44758	45860
3.0–3.4	17093	23021	33587	34543	660	34317	35313
3.4–3.8	13245	18203	26653	27533	491	27271	28188
3.8–4.2	10485	14641	21494	22274	374	22019	22833
4.2–4.7	9620	13362	20047	20438	333	20557	20964
4.7–5.2	10695	12950	19711	19926	311	20233	20457
5.2–6.0	...	12486	...	19341	287	...	19876
6.0–7.0	...	11720	...	18263	262	...	18781
7.0–8.3	...	10983	...	17213	235	...	17718
8.3–10.4	...	9727	...	15325	206	...	15782
10.4–13.7	...	8307	...	13147	174	...	13547
13.7–20.3	...	6526	...	10368	139	...	10686
20.3–23.1	...	1328	...	2114	29	...	2180
23.1–26.7	...	1163	...	1853	26	...	1910
26.7–31.7	...	962	...	1534	23	...	1579
31.7–39.0	...	941	...	1501	20	...	1549
39.0–50.6	...	802	...	1280	17	...	1321
50.6–72.2	...	574	...	917	14	...	945
72.2–91.7	...	239	...	382	6	...	394
91.7–125.8	...	162	...	259	5	...	267
125.8–200.0	...	145	...	232	4	...	240

[a] The rigidity bins at the spectrometer correspond to different intervals at the top of the payload and the top of the atmosphere due to ionization losses.
[b] Top of the atmosphere.

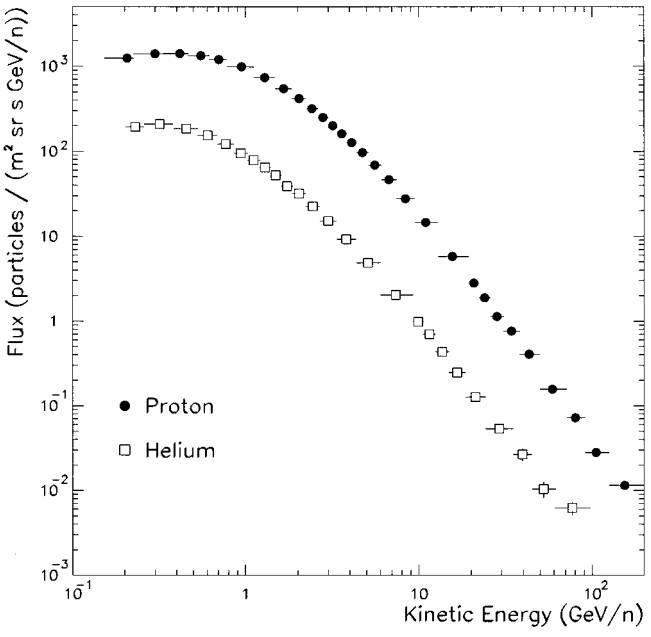

FIG. 9.—Particle fluxes at the top of the atmosphere as a function of kinetic energy per nucleon: *filled circle*, hydrogen nuclei spectrum; *empty square*, helium nuclei spectrum.

(Buckley et al. 1994) balloon experiment, which used a large ring-imaging Cerenkov telescope, and Japanese-American Cooperative Emulsion Experiment (JACEE; Asakimori et al. 1998) balloon experiments using nuclear emulsion detectors. Above 10 GeV a good agreement was obtained between these measurements, taking into account the errors, except the helium nuclei JACEE results that are systematically higher. At lower energies the effect of different solar modulations can clearly be seen. It has to be noticed that the LEAP and IMAX spectra, both for hydrogen and helium nuclei, have been deconvolved taking into account their spectrometer resolution. The results presented here have not been deconvolved.

We have chosen not to deconvolve the spectrum since the effect of the intrinsic spectrometer resolution on the measured spectra is smaller than the statistical errors, making a deconvolution difficult. Instead a systematic error has been included that accounts for the finite spectrometer resolution. This systematic error on the measured spectrum was estimated by assuming that the differential flux at high rigidities, where the finite spectrometer resolution has a measurable effect, is a power law in rigidity (R) of the type $AR^{-\gamma}$. Converting this into a deflection (D) spectrum gives a power law of the type $BD^{\gamma-2}$. This deflection spectrum was

TABLE 2

SUMMARY OF HELIUM NUCLEI RESULTS

Rigidity Bin at Spectrometer[a] (GV)	Observed Number of Events at Spectrometer	Extrapolated Number at Top of Payload	Extrapolated Number of Primary Events at TOA[b]
1.2–1.4	792	2840	3047
1.4–1.8	2876	7151	7690
1.8–2.2	3492	7085	7647
2.2–2.6	3449	6392	6916
2.6–3.0	2991	5308	5751
3.0–3.4	2473	4297	4659
3.4–3.8	2127	3660	3970
3.8–4.2	1790	3071	3331
4.2–4.7	1694	2909	3155
4.7–5.2	1585	2733	2965
5.2–6.0	1678	2918	3165
6.0–7.0	1565	2755	2989
7.0–8.3	1454	2604	2824
8.3–10.4	1304	2384	2586
10.4–13.7	1119	2096	2273
13.7–20.3	895	1715	1861
20.3–23.1	179	348	377
23.1–26.7	167	326	354
26.7–31.7	142	278	302
31.7–39.0	118	232	252
39.0–50.6	96	189	205
50.6–72.2	75	148	161
72.2–91.7	34	67	73
91.7–125.8	23	46	49
125.8–200.0	30	59	65

[a] The rigidity bins at the spectrometer correspond to different intervals at the top of the payload and the top of the atmosphere due to ionization losses.

[b] Top of the atmosphere.

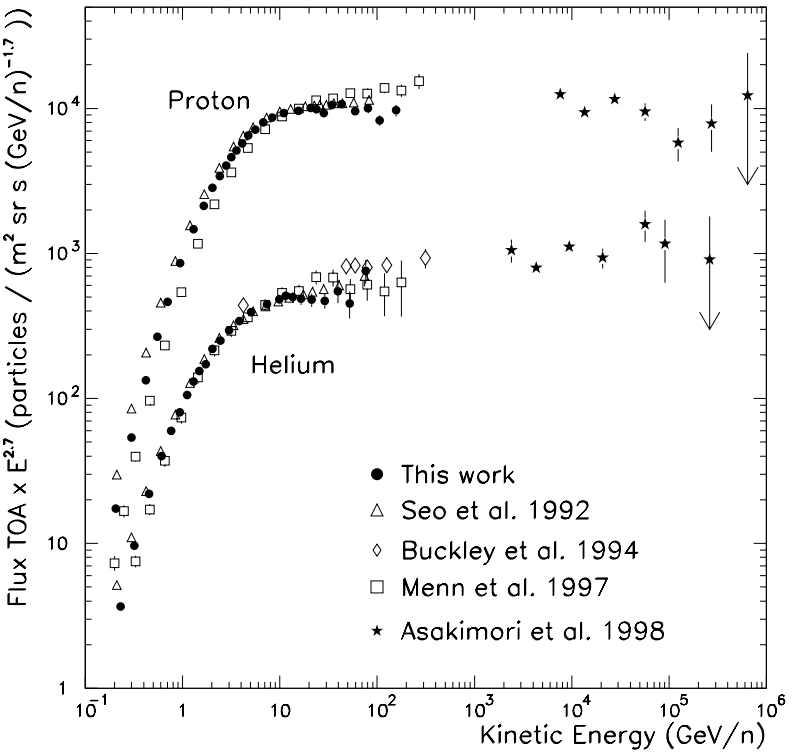

FIG. 10.—Hydrogen and helium nuclei fluxes at the top of the atmosphere as a function of the kinetic energy per nucleon for recent balloon-borne experiments: *filled circle*, this work; *empty triangle*, LEAP measurements (Seo et al. 1991); *empty diamond*, RICH measurements (Buckley et al. 1994); *empty square*, IMAX measurements (Menn et al. 1997); *star*, JACEE measurements (Asakimori et al. 1998). The fluxes are multiplied by $E^{2.7}$, where E is the kinetic energy in GeV per nucleon.

TABLE 3

MEASURED PROTON AND HYDROGEN FLUXES AT TOP OF ATMOSPHERE

Kinetic Energy at TOA[a] (GeV)	Mean Kinetic Energy at TOA (GeV)	Proton Flux at TOA[b] $(m^2\ sr\ s\ GeV)^{-1}$	Hydrogen Flux at TOA[b] $(m^2\ sr\ s\ GeV)^{-1}$
0.15–0.23	0.21	$(1.24 \pm 0.02) \times 10^3$	$(1.25 \pm 0.02) \times 10^3$
0.23–0.33	0.30	$(1.39 \pm 0.02) \times 10^3$	$(1.42 \pm 0.02) \times 10^3$
0.33–0.47	0.42	$(1.41 \pm 0.01) \times 10^3$	$(1.44 \pm 0.01) \times 10^3$
0.47–0.62	0.55	$(1.32 \pm 0.01) \times 10^3$	$(1.35 \pm 0.01) \times 10^3$
0.62–0.78	0.70	$(1.20 \pm 0.02) \times 10^3$	$(1.22 \pm 0.01) \times 10^3$
0.78–1.12.....	0.95	$(9.87 \pm 0.10) \times 10^2$	$(1.01 \pm 0.01) \times 10^3$
1.12–1.48.....	1.29	$(7.39 \pm 0.06) \times 10^2$	$(7.56 \pm 0.05) \times 10^2$
1.48–1.85.....	1.66	$(5.45 \pm 0.04) \times 10^2$	$(5.61 \pm 0.04) \times 10^2$
1.85–2.23.....	2.03	$(4.18 \pm 0.04) \times 10^2$	$(4.28 \pm 0.03) \times 10^2$
2.23–2.61.....	2.41	$(3.17 \pm 0.09) \times 10^2$	$(3.27 \pm 0.03) \times 10^2$
2.61–3.00.....	2.80	$(2.50 \pm 0.07) \times 10^2$	$(2.58 \pm 0.02) \times 10^2$
3.00–3.39.....	3.19	$(2.01 \pm 0.06) \times 10^2$	$(2.09 \pm 0.02) \times 10^2$
3.39–3.84.....	3.60	$(1.61 \pm 0.05) \times 10^2$	$(1.64 \pm 0.02) \times 10^2$
3.84–4.40	4.11	$(1.26 \pm 0.03) \times 10^2$	$(1.28 \pm 0.01) \times 10^2$
4.40–5.13.....	4.75	$(9.66 \pm 0.10) \times 10^1$	$(9.66 \pm 0.10) \times 10^1$
5.13–6.10	5.59	$(6.86 \pm 0.07) \times 10^1$	$(6.86 \pm 0.07) \times 10^1$
6.10–7.46.....	6.73	$(4.64 \pm 0.05) \times 10^1$	$(4.64 \pm 0.05) \times 10^1$
7.46–9.49.....	8.38	$(2.78 \pm 0.03) \times 10^1$	$(2.78 \pm 0.03) \times 10^1$
9.5–12.8	11.0	...	$(1.45 \pm 0.02) \times 10^1$
12.8–19.4.....	15.6	...	(5.82 ± 0.08)
19.4–22.2.....	20.7	...	(2.82 ± 0.08)
22.2–25.8.....	23.9	...	(1.88 ± 0.06)
25.8–30.8.....	28.1	...	(1.13 ± 0.04)
30.8–38.1.....	34.1	...	$(7.60 \pm 0.25) \times 10^{-1}$
38.1–49.7	43.2	...	$(4.06 \pm 0.15) \times 10^{-1}$
49.7–71.3.....	58.8	...	$(1.57 \pm 0.07) \times 10^{-1}$
71.3–90.8.....	80.0	...	$(7.21 \pm 0.49) \times 10^{-2}$
90.8–124.8	105.4	...	$(2.80 \pm 0.23) \times 10^{-2}$
124.8–199.1	154.3	...	$(1.15 \pm 0.11) \times 10^{-2}$

[a] Top of the atmosphere.
[b] The quoted errors are a combination of statistical and systematic errors.

then smeared by a Gaussian error distribution with a standard deviation parameter distribution deduced from the experimental data, peaked at 1/175 GV^{-1}. The smeared deflection distribution was then retransformed into a rigidity spectrum, and the ratio between the smeared spectrum and the input spectrum was used as a measure of the systematic error due to the finite spectrometer resolution. The error is only weakly dependent on the spectral index. The error due to the spectrometer resolution is small (less than 2%) up to 100 GV and reaches 5% at 200 GV. These systematic errors are significantly smaller than the statistical errors at corresponding rigidities, and they are added in quadrature to the statistical errors.

Assuming a power-law spectrum in kinetic energy per nucleon (i.e., a differential flux of the form $AE^{-\gamma}$, where γ is the spectral index and E the kinetic energy per nucleon) for the CAPRICE fluxes, a spectrum represented by $(1.1 \pm 0.1) \times 10^4\ E^{-2.73 \pm 0.06}$ particles $(m^2\ GeV\ sr\ s)^{-1}$ above 20 GeV for hydrogen nuclei and a spectrum represented by $(4.3 \pm 0.9) \times 10^2\ E^{-2.65 \pm 0.07}$ particles $(m^2\ GeV\ nucleon^{-1}\ sr\ s)^{-1}$ above 10 GeV $nucleon^{-1}$ for helium nuclei were found (for a discussion about bins, data points, and fit see Appendix). Ryan, Ormes, & Balasubrahmanyan (1972) observed spectral indices of 2.75 ± 0.03 for 50 to 1000 GeV hydrogen nuclei and 2.77 ± 0.05 for 20 to 800 GeV $nucleon^{-1}$ helium nuclei using an ionization calorimeter. If we instead assume a power-law spectrum in rigidity for the CAPRICE fluxes above 20 GV, the spectral indices become 2.79 ± 0.08 for hydrogen and 2.76 ± 0.08 for helium nuclei. Webber, Golden, & Stephens (1987) observed a spectral index of 2.7 ± 0.05, between 10 and 200 GV, for both hydrogen and helium nuclei in two balloon experiments in 1976 and 1979. Seo et al. (1991) reported spectral indices of 2.74 ± 0.02 for 10 to 100 GV hydrogen nuclei and 2.68 ± 0.03 for 10 to 200 GV helium nuclei. Menn et al. (1997) observed spectral indices (after solar demodulation) of 2.7 ± 0.06 for hydrogen nuclei and 2.76 ± 0.1 for helium nuclei between 20 and 150 GV. It should be noted that the error on the fitted parameters A and γ are strongly correlated, and a comparison between different measurements should be made by taking the full error matrix into account.

To verify that the spectrometer resolution has a negligible effect on the flux spectra when taking into account the errors, a similar fit to a power law of the hydrogen nuclei rigidity spectrum was made in the interval 20–50, 20–100, and 20–200 GV, resulting in a spectral index of 2.69 ± 0.07, 2.75 ± 0.06, and 2.79 ± 0.08, respectively. The fitted indices agree within less than 1 σ, indicating that the spectrometer resolution has a negligible influence on the flux spectra when taking into account the errors.

3.5. *Systematic Errors*

Some systematic errors originating from the determination of the detector efficiencies have already been discussed above. The tracking efficiency was estimated to be determined with a precision of 5%, and the RICH and the

TABLE 4

MEASURED HELIUM NUCLEI FLUX AT TOP OF ATMOSPHERE

Kinetic Energy at TOA[a] (GeV nucleon^{-1})	Mean Kinetic Energy at TOA (GeV nucleon^{-1})	Helium Nuclei Flux at TOA[b] (m^2 sr s GeV nucleon^{-1})$^{-1}$
0.20–0.26	0.23	$(1.94 \pm 0.08) \times 10^2$
0.26–0.38	0.32	$(2.10 \pm 0.04) \times 10^2$
0.38–0.53	0.46	$(1.84 \pm 0.03) \times 10^2$
0.53–0.69	0.61	$(1.54 \pm 0.03) \times 10^2$
0.69–0.85	0.77	$(1.22 \pm 0.02) \times 10^2$
0.85–1.03	0.94	$(9.49 \pm 0.20) \times 10^1$
1.03–1.21	1.12	$(7.86 \pm 0.18) \times 10^1$
1.21–1.39	1.30	$(6.48 \pm 0.16) \times 10^1$
1.39–1.60	1.49	$(5.23 \pm 0.13) \times 10^1$
1.60–1.87	1.73	$(3.90 \pm 0.10) \times 10^1$
1.87–2.22	2.04	$(3.20 \pm 0.08) \times 10^1$
2.2–2.7	2.4	$(2.25 \pm 0.06) \times 10^1$
2.7–3.4	3.0	$(1.51 \pm 0.04) \times 10^1$
3.4–4.4	3.8	(9.24 ± 0.26)
4.4–6.0	5.1	(4.90 ± 0.15)
6.0–9.3	7.4	(2.04 ± 0.07)
9.3–10.7	9.9	$(9.80 \pm 0.74) \times 10^{-1}$
10.7–12.5	11.5	$(6.97 \pm 0.54) \times 10^{-1}$
12.5–15.0	13.6	$(4.33 \pm 0.36) \times 10^{-1}$
15.0–18.6	16.6	$(2.47 \pm 0.23) \times 10^{-1}$
18.6–24.4	21.2	$(1.26 \pm 0.13) \times 10^{-1}$
24.4–35.2	28.9	$(5.33 \pm 0.62) \times 10^{-2}$
35.2–45.0	39.5	$(2.67 \pm 0.46) \times 10^{-2}$
45.0–62.0	52.2	$(1.04 \pm 0.22) \times 10^{-2}$
62.0–99.1	76.7	$(6.20 \pm 1.20) \times 10^{-3}$

[a] Top of the atmosphere.

[b] The quoted errors are a combination of statistical and systematic errors.

scintillator efficiencies to 2% or better.

Another possible systematic error was the trigger efficiency. The trigger was a fourfold coincidence between two photomultiplier tubes with signals in the top and bottom scintillator paddles, respectively. The threshold of each photomultiplier tube was set high enough to eliminate noise, but low enough to be very close to 100% efficient to minimum ionizing particles. The fraction of each trigger combination was compared with the simulated fraction taking into account the position of each paddle and the magnetic field. The agreement between the simulated fraction of trigger combinations and the measured ones was good, and the conclusion was that the trigger efficiency was higher than 99% and that a possible systematic error due to the trigger efficiency is less than 1%.

The geometrical factor was obtained with simulation techniques (Sullivan 1971) using two different methods to trace the particles. In the first method the track-fitting algorithm used in the analysis was used to trace the particle through the spectrometer. In the second, the GEANT simulation program (Brun et al. 1994) was used to trace the particles. Both methods gave the same result within 1% at all rigidities discussed in this paper. The result was cross checked using a numerical integration calculation of the geometrical factor, which agrees with the previous results within 2% above 0.5 GV and 5% below 0.5 GV. From this it was estimated that the geometrical factor was known with a precision of better than 5% between 0.4 and 0.5 GV and better than 2% for rigidities higher than 0.5 GV.

In the hydrogen analysis it was assumed that all particles had the mass of a proton. This introduces a systematic error when converting rigidity to kinetic energy using the mass of a proton, since some hydrogen events are deuterons. The assumption that the deuteron fraction is of the order of 2% (Reimer et al. 1995) gives a systematic error on the kinetic energy of 2% at 0.1 GeV decreasing to 0.5% and less above 3 GeV. Similarly, assuming that the ^{3}He fraction in the helium nuclei sample is of the order of 15% (Reimer et al. 1998) makes the systematic error on the kinetic energy per nucleon 4% at 0.1 GeV nucleon^{-1} decreasing to less than 1% above 3 GeV nucleon^{-1}.

It was assumed that all interactions above the tracking system that produced new charged particles were rejected by the selection criteria on the RICH and the top scintillator. The amount of material above the tracking system (including the dome, but excluding the bar and the rigging equipment) was 9 g cm^{-2} or of the order of 10% of an interaction length. Thus, even if 10% of the strong interaction events were not rejected by the selection criteria, this would only affect the measured flux on the percent level.

The numbers of particles measured at the spectrometer were corrected for losses in the spectrometer and the atmosphere, as well as secondary production in the atmosphere above the spectrometer. Simulations of proton ionization energy losses in the spectrometer show a 20% uncertainty on the proton flux at 0.2 GeV, decreasing to less than 1% above 0.4 GeV. The amount of secondary particles in the measured data was estimated to be 40% at 0.5 GV decreasing to 5% at 1 GV and between 1% and 2% above 3 GV. The estimate of the atmospheric secondaries was made by repeating the calculations of Papini et al. (1996) using the spectra obtained in this experiment, and we do not expect the systematic errors in this estimate to be much larger than 5%. To be conservative, a 10% uncertainty was assumed on

these calculations, which has a negligible (<1%) influence on the results except for rigidities below 1 GV, where the systematic error due to secondary production in the atmosphere can be up to 7% at 0.5 GV. The propagation of particles from the spectrometer to the top of the atmosphere included corrections for losses in the atmosphere (3.9 ± 0.4 g cm^{-2}) and above the tracking system (9 ± 1 g cm^{-2}), which was estimated to be 15% above 2 GV and decreasing at lower rigidities. Assuming a 10% uncertainty on the cross sections used in these calculations results in a systematic error on the results of less than 2% from losses in the payload and the residual atmosphere. The systematic errors are similar for the helium nuclei.

From this discussion, and assuming that the systematic errors discussed above are uncorrelated, we estimated that the measurements can include systematic uncertainties that are rigidity dependent but less than 20% below 1 GV decreasing to less than 10% above 5 GV.

3.6. *Solar Modulation*

The solar modulation was studied to compare the CAPRICE hydrogen and helium nuclei spectra with other measurements at low energies. In this paper we have made use of the spherically symmetric model suggested for solar modulation by Gleeson & Axford (1968). Thus, we assumed that the differential intensity $J(r, E, t)$ at a radial distance r from the Sun, for a total energy E of the cosmic-ray particle and time t, is related to the time-independent interstellar intensity $J(\infty, E)$ as

$$J(r, E, t) = \frac{E^2 - E_0^2}{[E + \Phi(t)]^2 - E_0^2} J[\infty, E + \Phi(t)] , \qquad (2)$$

with E_0 being the rest energy (mass) of the particle and Φ a parameter that can be interpreted as the energy loss experienced by the cosmic-ray particle when approaching the Earth from infinity. Assuming that the diffusion of the particles in the magnetic field is described by a diffusion coefficient k separable with a form $k = k_1(r)R\beta$ (R rigidity and β velocity of the particle), then Φ is related to the solar modulation parameter

$$\phi = \int_{r_1}^{r_b} \frac{v}{3k_1} dr , \qquad (3)$$

with r_b heliospheric boundary distance and v solar wind speed, by the expression $\Phi = |Z| e\phi$ (Gleeson & Axford 1968).

Figure 11 shows $J(r, E, t)/R^2$ as a function of kinetic energy divided by the charge (Ze) for hydrogen and helium nuclei (Gleeson & Axford 1968) as obtained with this work and as given by LEAP (Seo et al. 1991) and IMAX (Menn et al. 1997). As shown by Gleeson & Axford (1968), the displacement along the abscissa, taken with reversed sign, is the difference between the solar modulation parameters for the three measurements. Note that the displacement between the curves for hydrogen nuclei is constant over the energy range shown and that the solar modulation parameter in this experiment is about 100 MV higher than for LEAP and about 200 MV lower than for IMAX. The same displacement was obtained from the curves for helium nuclei between CAPRICE and LEAP data, while the relations do not hold for the IMAX helium nuclei data. From the published modulation parameters of these two experiments ($\phi = 500$ MV for LEAP [Seo et al. 1991] and $\phi = 800$ MV for IMAX [Menn et al. 1997]) we conclude that the CAPRICE solar modulation parameter ϕ was ~ 600 MV.

An absolute number for the solar modulation parameter for the CAPRICE hydrogen and helium nuclei data was obtained following the same method as adopted by the LEAP and IMAX experiments. The energy spectra were converted to rigidity spectra. A power-law spectrum in rigidity was then fitted to equation (2) to obtain the value of ϕ. The best fit of the CAPRICE data was obtained with a parameter $\phi = 710$ MV for protons and $\phi = 840$ MV for helium nuclei. The difference between the parameter values for protons and helium nuclei indicates that the assumption of having the same spectral shape of a power law in rigidity for the interstellar spectra may not be completely correct. However, it is important to point out that the solar modulation parameter obtained in this way is dependent on the choice of the parametrization of the interstellar flux.

A different value of ϕ for the CAPRICE flight was found by Golden et al. (1995), who used data from the neutron monitor counter Climax (Simpson & Pyle 1996).[2] The parameter ϕ for the CAPRICE flight using this method was found to be 500 MV. However, as shown recently by the Balloon-borne Experiment with a Superconducting Magnet Spectrometer (BESS; Matsunaga 1996) and the IMP8 (Seo 1996) collaborations the proton flux is a more sensitive probe of the solar modulation parameter at energies around 1 GeV at the top of the atmosphere than a neutron monitor counter on the ground. This is illustrated by the following data. The Climax neutron counter values (Simpson & Pyle 1996) for the time of the LEAP (year = 87, month = 08, day = 21), IMAX (920716), CAPRICE (940808), BESS93 (930726), BESS94 (940731), BESS95 (950725), IMP8-93

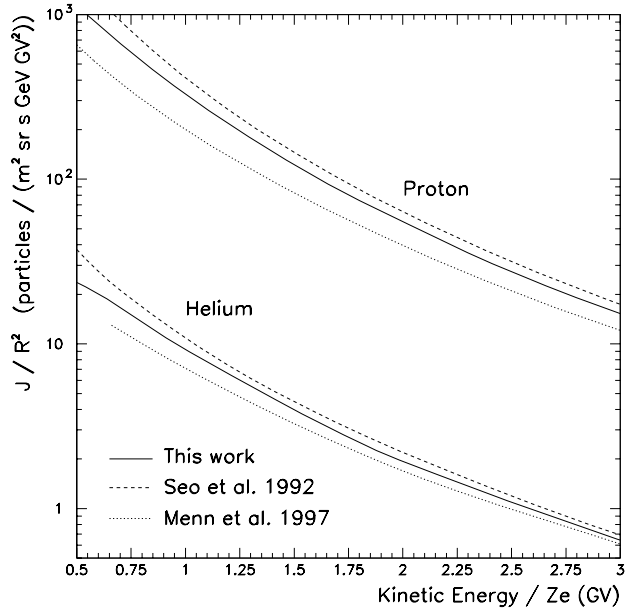

FIG. 11.—Hydrogen and helium nuclei fluxes (J) divided by rigidity squared versus kinetic energy divided by the charge (Ze). *Solid line*, this analysis; *dashed line*, LEAP measurements (Seo et al. 1991); *dotted line*, IMAX measurements (Menn et al. 1997). The constant displacement, for both species, between the three curves is attributed to the difference between the values of the three solar modulation parameters.

[2] National Science Foundation grant ATM-9420790, http://odysseus.uchicago.edu/NeutronMonitor/neutron.html.

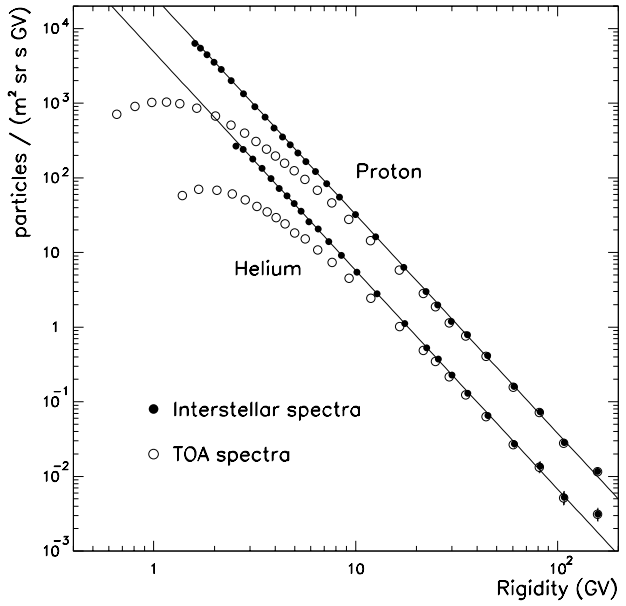

FIG. 12.—CAPRICE hydrogen and helium nuclei spectra as a function of rigidity: *empty circle*, top of the atmosphere; *filled circle*, interstellar for a solar modulation parameter $\phi = 710$ MV and 840 MV, respectively. The solid lines are fits according to eqs. (4) and (5).

(930714-930809), IMP8-94 (940719-940814), and IMP8-95 (950715-950809) were nearly constant. They were on average $(4.09 \pm 0.03) \times 10^5$, $(3.89 \pm 0.03) \times 10^5$, $(4.11 \pm 0.03) \times 10^5$, $(4.09 \pm 0.05) \times 10^5$, $(4.05 \pm 0.03) \times 10^5$, $(4.13 \pm 0.05) \times 10^5$, $(4.05 \pm 0.08) \times 10^5$, $(4.08 \pm 0.08) \times 10^5$, $(4.14 \pm 0.06) \times 10^5$ counts hr^{-1}, during the respective measurements. Note that the errors quoted here are based on the fluctuations of the hourly rate over the period of observation. Yet the BESS collaboration measures a significant increase in the proton flux around 1 GeV

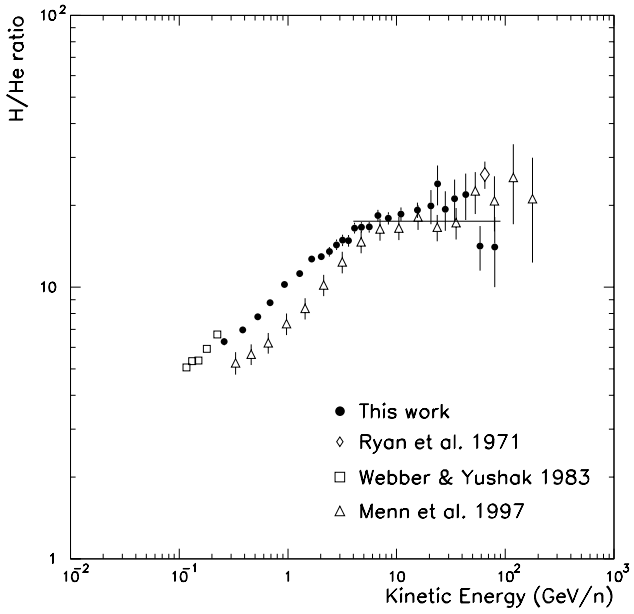

FIG. 13.—Hydrogen to helium nuclei flux ratio at the top of the atmosphere as a function of kinetic energy per nucleon. The experimental data are as follows: *filled circle*, this work; *empty diamond*, Ryan et al. (1972); *empty square*, Webber & Yushak (1983); *empty triangle*, Menn et al. (1997).

between the 1993 and the 1995 measurements (Matsunaga 1996). This increase is also confirmed by the IMP8 (Seo 1996) measurements and the LEAP (Seo et al. 1991), IMAX (Menn et al. 1997), and CAPRICE (this paper) measurements.

As an example, expressing the interstellar spectra in the form of a power law in rigidity and using $\phi = 710$ MV for hydrogen nuclei and $\phi = 840$ MV for helium nuclei, a fit between 1.7 and 200 GV of the interstellar hydrogen nuclei spectrum results in

$$J(R) = (2.72 \pm 0.02) \times 10^4 R^{-2.928 \pm 0.004} \text{ (m}^2 \text{ sr s GV)}^{-1} , \quad (4)$$

and the interstellar helium nuclei spectrum

$$J(R) = (4.90 \pm 0.08) \times 10^3 R^{-2.93 \pm 0.01} \text{ (m}^2 \text{ sr s GV)}^{-1} , \quad (5)$$

These spectra are shown in Figure 12 together with the spectra at the top of the atmosphere. The previous estimates of the interstellar hydrogen nuclei flux have often been done by fitting a power law to the high-energy measurements of the hydrogen nuclei spectrum at Earth assuming that the solar modulation has no effect at high energies. However, the point we want to make here, which is shown in Figure 12, is that the effect of the solar modulation is appreciable also at rigidities up to 50 GV and measurably changes the index of the power-law fit making the interstellar spectra steeper.

3.7. *Hydrogen to Helium Nuclei Ratio*

It can be seen from Figure 12 that the ratio of hydrogen to helium nuclei at the top of the atmosphere is nearly constant between 5 and 200 GV with a value of 6.1 ± 0.1. Below 5 GV this ratio increases as a result of different magnitude of solar modulation for these two species of nuclei. The mass to charge ratios of these two elements are way too different and therefore their flux ratio is a good probe of cosmic-ray propagation in the Galaxy and their injection spectra. We have shown in Figure 13 the hydrogen to helium ratio at the top of the atmosphere as a function of kinetic energy per nucleon. Our results show that the proton to helium ratio is nearly constant above 4 GeV nucleon^{-1} and its value is 17.5 ± 0.5 as shown by the solid line. As a comparison, we have shown data by Ryan et al. (1972) and Menn et al. (1997). Although there is a large spread in the data points, one finds a general agreement between these measurements. The differences in the experimental data at low energies are due to solar modulation. We have also shown the data by Webber & Yushak (1983), which were taken in 1977 July close to the 1976 solar minimum. This set of data at very low energies follows the trend of our results. One striking feature that we see from this figure is the change of ratio around 4 GeV nucleon^{-1}. This change is also clearly seen in the data by Menn et al. (1997), as well as in the work by Seo et al. (1991). This transition may have important implications on the propagation of cosmic rays.

4. DISCUSSION AND CONCLUSION

The CAPRICE apparatus allows an unprecedented determination of the detector efficiencies, as clean samples of individual particle types could be selected by independent sets of detectors to determine the efficiency of each instrument with good accuracy. This is very important

when measuring hydrogen and helium nuclei fluxes since the measurements are normally not limited by statistical errors or contamination, but by systematic errors that are mainly due to the uncertainties of the detector efficiencies.

Furthermore, clear separation between protons and deuterons was possible with this instrument between 0.4 and 5 GV, which allowed the proton component of the hydrogen spectrum to be determined for the first time over this rigidity range. The deuteron flux will be the topic of a separate paper. In this regard we would like to point out that the efficiencies are estimated under the assumption that all unit charged particles selected are protons. This results in a negligible error in the hydrogen flux but will result in a large systematic error on the difference between the hydrogen flux and the proton flux. Therefore, we do not recommend interpreting the difference between the hydrogen flux and the proton flux presented in this paper as a measurement of the deuteron flux.

The finite spectrometer resolution has not been deconvolved from the measured spectra since its effect on the energy spectra is smaller than the statistical errors (at least up to 200 GeV) making a deconvolution difficult. Instead, we have estimated the systematic error due to the finite spectrometer resolution and added it in quadrature to the statistical error.

An important point made in this paper is the influence of the solar modulation on the energy spectra at high energies. Previously, the interstellar flux has normally been determined by fitting a power law in kinetic energy to the flux measured at the top of the atmosphere assuming that the solar modulation is negligible above 10 GeV. We have shown that the solar modulation has a small but important effect up to at least 50 GeV. The spectra obtained after demodulating also the high-energy measurements are significantly steeper than what was previously obtained. It is interesting to note that a fit to a power law in rigidity gives a slightly, but measurably, higher index than a power-law fit in kinetic energy.

We obtained a value of 6.1 ± 0.1 as the ratio of hydrogen to helium nuclei between 5 and 200 GV and a value of 17.5 ± 0.5 in the energy region between 4 and 90 GeV nucleon^{-1}.

This work was supported by NASA grant NAGW-110; The Istituto Nazionale di Fisica Nucleare, Italy; the Agenzia Spaziale Italiana; DARA and DFG in Germany; EU SCIENCE; the Swedish National Space Board; and the Swedish Council for Planning and Coordination of Research. We wish to thank the National Scientific Balloon Facility and the NSBF launch crew that served in Lynn Lake. We would also like to acknowledge the essential support given by the CERN TA-1 group and the technical staff of NMSU and of INFN.

APPENDIX

BINNING AND CENTERING OF DATA POINTS

As described in § 3.4, the rigidity range for protons, hydrogen, and helium nuclei analysis was split in bins of 50 MV width between 0.4 GV (1.2 GV for helium nuclei analysis) and 4 GV, and for higher rigidities in bins with constant width in deflection of 0.003 GV^{-1} (half of the inverse of the MDR). Then the number of data points was reduced merging them together except for the last three points. Above 10 GV the widths of the bins become too large to assume a linear variation of the spectra over the bins. Hence, plotting the data points using the barycenter method (also called the weighted average method) results in an incorrect representation of the spectra. As pointed out by Lafferty & Wyatt (1995) a more correct way of presenting the data over large width bins is to use the abscissa points for which the measured data points lie on the true spectrum [$f(x)$], i.e., the abscissa values ($x_{\rm lw}$ means large width bins, using Lafferty & Wyatt 1995 notation) at which the measured spectrum is equal to the expectation value of the true spectrum. This can be expressed as

$$f(x_{\rm lw}) = \frac{1}{x_2 - x_1} \int_{x_1}^{x_2} f(x)\, dx \ , \tag{A1}$$

with $x_2 - x_1$ the width of the bin and x_1 and x_2 the lower and upper limit of the bin, respectively. For a power-law spectrum [$f(x) = Ax^{-\gamma}$] $x_{\rm lw}$ becomes

$$x_{\rm lw} = \left[\frac{x_2^{1-\gamma} - x_1^{1-\gamma}}{(x_2 - x_1)(1-\gamma)} \right]^{-1/\gamma} . \tag{A2}$$

Above 10 GV both the hydrogen and helium nuclei spectra are well approximated by power laws; thus, equation (A2) can be used. The spectral index γ was obtained iteratively: the spectra were fitted with a power law with abscissa points given by the barycenter method, the resulting γ was used to evaluate new abscissa points with equation (A2), and a new fit was performed resulting in a new spectral index that was used again to estimate $x_{\rm lw}$. This proceeded until the resulting spectral index differed from the previous one less than 0.1%. The data points above 20 GV, presented in this work, have been centered according to this technique.

REFERENCES

Asakimori, K., et al. 1998, ApJ, 502, 278
Barbiellini, G., et al. 1996a, Nucl. Instr. Meth., A371, 169
———. 1996b, A&A, 309, L15
———. 1997a, Proc. 25 Int. Cosmic-Ray Conf. (Durban), 3, 369
———. 1997b, Proc. 25 Int. Cosmic-Ray Conf. (Durban), 3, 377
Bocciolini, M., et al. 1996, Nucl. Instr. Methods Phys. Res., A370, 403
Boezio, M., et al. 1997, ApJ, 487, 415
Brun, R., et al. 1994, Detector Description and Simulation Tool, CERN program library
Buckley, J., Dwyer, J., Mueller, D., Swordy, S., & Tang, K. K. 1994, ApJ, 429, 736
Carlson, P., et al. 1994, Nucl. Instr. Methods Phys. Res., A349, 577
Circella, M., et al. 1997, Proc. 25 Int. Cosmic-Ray Conf. (Durban), 7, 117
Gaisser, T. K., & Schaefer, R. K. 1992, ApJ, 394, 174

Gaisser, T. K., Honda, M., Kasahara, K., Lee, H., Midorikawa, S., Naumov, V., & Stanevet, T. 1996, Phys. Rev. D, 54, 5578
Gleeson, L. J., & Axford, W. I. 1968, ApJ, 154, 1011
Golden, R. L., et al. 1978, Nucl. Instr. Methods Phys. Res., 148, 179
———. 1991, Nucl. Instr. Methods Phys. Res., A306, 366
———. 1995, Proc. 26 Int. Cosmic-Ray Conf. (Rome), 4, 828
———. 1996, ApJ, 457, L103
Hof, M., et al. 1994, Nucl. Instr. Methods Phys. Res., A345, 561
———. 1996, ApJ, 467, L33
Lafferty, G. D., & Wyatt, T. T. 1995, Nucl. Instr. Methods Phys. Res., A355, 541
Matsunaga, H. 1996, in Proc. Sixth Workshop on Balloon-borne Experiment with a Superconducting Magnet Spectrometer, ed. A. Yamamoto & T. Yoshida (Tokyo: Internat. Center Elementary Particle Phys.)
Menn, W., et al. 1997, Proc. 25 Int. Cosmic-Ray Conf. (Durban), 3, 409
Mitchell, J., et al. 1996, Phys. Rev. Lett., 76, 3057
Papini, P., Grimani, C., & Stephens, S. A. 1996, Nuovo Cimento, 19, 367
Pfeifer, Ch., Roesler, S., & Simon, M. 1996, Phys. Rev. C, 54, 2, 882
Reimer, O., et al. 1995, Proc. 26 Int. Cosmic-Ray Conf. (Rome), 2, 614
———. 1998, ApJ, 496, 490
Ryan, M. J., Ormes, J. F., & Balasubrahmanyan, V. 1972, Phys. Rev. Lett., 28, 985
Seo, E. S. 1996, in Proc. Sixth Workshop on Balloon-borne Experiment with a Superconducting Magnet Spectrometer, ed. A. Yamamoto & T. Yoshida (Tokyo: Internat. Center Elementary Particle Phys.)
Seo, E. S., Ormes, J. F., Streitmatter, R. E., Stochaj, S. J., Jones, W. V., Stephens, S. A., & Bowen, T. 1991, ApJ, 378, 763
Simpson, J. A., & Pyle, K. R. 1996, Space Physics Data System (Univ. Chicago)
Stephens, S. A. 1981, Proc. 27 Int. Cosmic-Ray Conf. (Paris), 4, 282
———. 1997, Astropart Phys., 6, 229
Sullivan, J. D. 1971, Nucl. Instr. Methods Phys. Res., 95, 5
Webber, W. R., Golden, R. L., & Stephens, S. A. 1987, Proc. 20 Int. Cosmic-Ray Conf. (Moscow), 1, 325
Webber, W. R., & Yushak, S. M. 1983, ApJ, 275, 391
Weber, N. 1997, Ph.D. thesis, Royal Inst. Tech., Stockholm